

Simulating flexible polymers in a potential of randomly distributed hard disks

Sebastian Schöbl, Johannes Zierenberg, and Wolfhard Janke

*Institut für Theoretische Physik,
Universität Leipzig, Postfach 100920,
D-04009 Leipzig, Germany*

We perform equilibrium computer simulations of a two-dimensional pinned flexible polymer exposed to a quenched disorder potential consisting of hard disks. We are especially interested in the high-density regime of the disorder, where subtle structures such as cavities and channels play a central role. We apply an off-lattice growth algorithm proposed by Garel and Orland [J. Phys. A **23**, L621 (1990)], where a distribution of polymers is constructed in parallel by growing each of them monomer by monomer. In addition we use a multicanonical Monte Carlo method in order to cross-check the results of the growth algorithm. We measure the end-to-end distribution and the tangent-tangent correlations. We also investigate the scaling behavior of the mean square end-to-end distance in dependence of the monomer number. While the influence of the potential in the low-density case is merely marginal, it dominates the configurational properties of the polymer for high densities.

I. INTRODUCTION

Transport phenomena and polymers in porous media [1–3] already required theoretical models of polymers in disordered systems in the 1980s. Since then these problems have been widely discussed [4–14]. In this paper we apply two algorithms for simulating the equilibrium properties of a flexible polymer in a disorder potential of hard disks. We are especially interested in the high-density regime of the disorder, which gives rise to structures that are hard to tackle with common methods. We place the disks of the potential randomly onto the sites of a square lattice, so that, e.g., the distance between nearest neighbors can be controlled. This somewhat artificial arrangement, which causes, e.g., narrow channels and small cavities (see Sec. II B), was chosen in order to investigate the influence of those structures on flexible polymers and to test the methods we use. In forthcoming work we want to apply them to the more general biophysically inspired problem of semiflexible polymers in crowded media where the disorder is irregular and possibly correlated (e.g., a hard-disk fluid) [15]. We access this problem by applying and comparing two algorithms. One algorithm is an off-lattice growth algorithm [16]. Growth algorithms are intensively used for lattice polymer systems [17–20] whereas they are rarely applied for the off-lattice case. The other method is the multicanonical Monte Carlo method [21–23], which is a common instrument for handling systems with rough energy landscapes. It has already proven to be very efficient for polymeric systems [24]. Throughout our analysis we found perfect agreement of the two methods except for some special case of parameters. We will discuss the merits and drawbacks of these methods in Sec. V.

The rest of the paper is organized as follows: In Sec. II we describe our polymer model and how the disorder is realized. Then, in Sec. III, we describe the algorithms. At the end of this section, we specify the parameters for our simulations. In Sec. V we show our findings. A conclusion is given in Sec. VI.

II. POLYMER MODEL AND DISORDER

We simulate a polymer exposed to a disorder landscape consisting of hard disks. The polymer is pinned at one end. We carry out the quenched disorder average as follows: We choose a random starting point for each disorder realization and run an equilibrium computer simulation. We estimate averages from the resulting distribution of polymer configurations. Averages for a single disorder realization are written in angular brackets $\langle \dots \rangle$. This is done for all disorder realizations and the quenched average is calculated from this by averaging over the measured values of the single disorder realizations. The quenched average is written as $[\langle \dots \rangle]$. The parameters we use for our simulations are described in detail in Sec. IV.

A. Polymer model

Our polymer model is a freely jointed chain. Effectively, this is a bead-stick model whose contour is defined by $N+1$ beads at positions \mathbf{r}_i connected by bonds of fixed length b . Therefore the contour has the fixed length $L = Nb$. The polymer chain is a phantom chain, which means that there is no monomer-monomer interaction except for the fixed distance between bonded monomers. The connecting line of bonded monomers defines unit vectors $\mathbf{t}_i = (\mathbf{r}_{i+1} - \mathbf{r}_i)/b$. Our methods can easily be adapted to other polymer models. In a forthcoming work, we will extend it to involve bending energy.

B. Disorder potential

The background potential consists of hard disks with diameter σ_i , which interact with the monomers of the polymer via hard-core repulsion. The interaction poten-

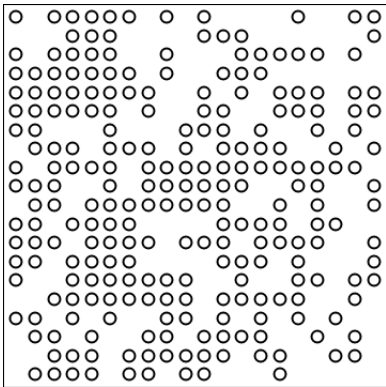


Figure 1. Hard-disk disorder configuration with site occupation probability $p = 0.64$.

tial between monomers and disks is thus described by

$$V = \begin{cases} \infty & \text{for } d < \sigma_i/2 \\ 0 & \text{else} \end{cases} \quad (1)$$

where d is the distance between a monomer and the center of a disk of the background potential (no monomer volume).

The disks are placed onto the sites of a square lattice with a lattice constant chosen to be of the order of the disk diameter. This arrangement was chosen in order to be able to control the distance between neighboring disks. In such a disorder landscape the algorithms can be well tested. The algorithms can then easily be applied to other potentials such as, e.g., hard-disk fluids.

In order to generate random configurations we occupy each lattice site with the same probability. The resulting structure mimics – to a certain extent – the structure of a diluted square lattice. Figure 1 shows an example configuration of hard disks with site occupation probability $p = 0.64$.

III. ALGORITHMS

Application of a standard Markov chain Monte Carlo (MCMC) method based upon the Metropolis algorithm [25], that is, building up an initial polymer chain and then updating it in order to sample the configuration space, did not work well for our purposes. The updates included only the changes of angles between neighboring bonds, but even more refined update moves such as pivot moves would certainly not work efficiently in this situation. For a highly dense background, these methods result in either a diverging autocorrelation time or a rejection rate that makes it impossible to create enough configurations to compute observables.

A. Method 1: Chain growth algorithm

Following the approach proposed by Garel and Orland [16], we generate ensembles of pinned polymers by placing $M \sim 10^5$ seeds at a randomly chosen site and simultaneously growing them, monomer by monomer, until the desired degree of polymerization is reached. After each growth step, we attain thermal equilibration by replicating or deleting chains according to their Boltzmann weight (0 if the chain happens to collide with a background obstacle, 1 otherwise). To avoid an exponential decline in the chain population, a population control parameter is introduced that keeps the total number of ensemble members approximately constant (see Fig. 2). Prior to the proper growth process, the overall number of chains in this step is estimated. The population control parameter is the ratio of the initial number of seeds and the estimated number of chains in the next step. The weight for each chain is multiplied by the population control parameter. Other types of polymer interaction such as bending energy can be treated similarly by using different Boltzmann weights.

B. Method 2: Multicanonical Monte Carlo algorithm

In order to avoid trapping problems of the polymer in a system with hard disks, we can treat the excluded areas as finite potentials. That way, the polymer is allowed to access the previously forbidden disks with the Boltzmann probability, depending on the energy penalty from monomers located on the disks. This approach allows for a multicanonical simulation [21, 22] in the amplitude parameter of the disk potential, opening the possibility of reproducing the limiting cases of a free polymer (zero amplitude) and a polymer in hard disk disorder (infinite amplitude).

In general, the total energy of a polymer may be defined as the sum of the intra-polymer energy E_{poly} and the potential energy kE_{pot} , where E_{pot} is the sum of monomers located on disks and k is the amplitude of the disk potential in energy units. While the intra-polymer energy is a continuous quantity, the potential energy is discrete. The canonical partition function is given as the sum over all polymer configurations $\{x_i\}$

$$Z_{\text{can}} = \sum_{\{x_i\}} e^{-\beta(E_{\text{poly}}(\{x_i\}) + kE_{\text{pot}}(\{x_i\}))}. \quad (2)$$

In our case, this simplifies even more as we only consider a flexible polymer with vanishing intra-polymer energy E_{poly} , but the method also works for polymers with interactions. It is possible to separate the Boltzmann factor into contributions of the intra-polymer energy and of the potential energy. Replacement of the Boltzmann factor of the potential energy by a variable weight factor results

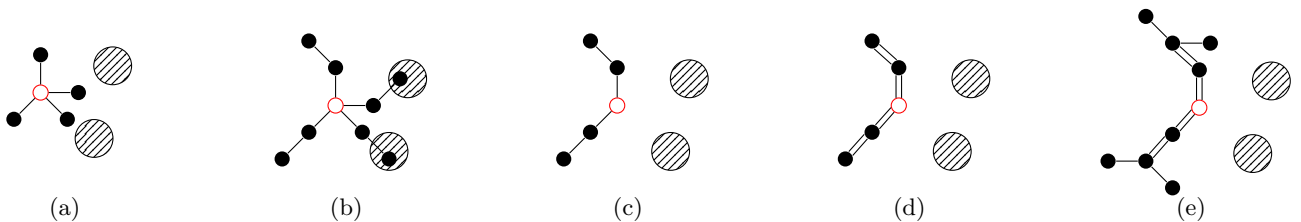


Figure 2. (Color online) (a) Initial growth in four different directions corresponds to four different polymer chains of length 1 starting from the seed marked by the red open circle. (b) Each of the chains is grown by one monomer. Two of the chains overlap with a disk of the background potential. The weight of these chains is 0. (c) The chains with weight 0 are removed from the population. (d) The population control parameter keeps the overall number of chains approximately constant. On average each of the remaining chains is thus replicated and now exists twice in the population. (e) Each of the chains is grown independently by one more monomer.

in our multicanonical partition function

$$Z_{\text{muca}} = \sum_{\{x_i\}} e^{-\beta E_{\text{poly}}(\{x_i\})} W(E_{\text{pot}}(\{x_i\})). \quad (3)$$

Independent on the choice of the weights, the canonical expectation values can always be recovered by

$$\langle O \rangle_{\text{can}} = \frac{\langle OW^{-1}(E_{\text{pot}}(\{x_i\}))e^{-\beta k E_{\text{pot}}(\{x_i\})} \rangle_{\text{muca}}}{\langle W^{-1}(E_{\text{pot}}(\{x_i\}))e^{-\beta k E_{\text{pot}}(\{x_i\})} \rangle_{\text{muca}}}. \quad (4)$$

Now, the weights may be adjusted such that states that initially occur frequently are suppressed, while states with rarely occurring potential energies are amplified. The weights are iterated in equilibrium simulations until the resulting histogram of the potential energy $H(E_{\text{pot}})$ is flat and thus configurations with different numbers of monomers located on hard disks appear with the same rate, allowing the polymer to cross over previous barriers of hard disks. This may be achieved in different ways [23]. In our case we start with the Boltzmann weights in Eq. (2) with $\beta k = 1$ and after each equilibrium simulation we recalculate the weights with

$$W^{(n+1)}(E_{\text{pot}}) = \frac{W^{(n)}(E_{\text{pot}})}{H^{(n)}(E_{\text{pot}})}. \quad (5)$$

This simple weight update already leads to a quick convergence to flat histograms. As the first histogram may be narrow, it is of advantage to begin with small statistics, increasing the number of updates in each iteration upon a chosen threshold.

In the end, the resulting weights are used to perform a final simulation. The desired observables are obtained by reweighing the final time series, meaning that the weights with which the observables were measured are replaced by the weights with which they would appear in the canonical ensemble. With proper normalization this gives

$$\langle O \rangle_{\text{can}} \approx \bar{O}_{\text{can}} = \frac{\sum_i \frac{e^{-\beta k E_{\text{pot},i}}}{W(E_{\text{pot},i})} O_i}{\sum_i \frac{e^{-\beta k E_{\text{pot},i}}}{W(E_{\text{pot},i})}}. \quad (6)$$

IV. SIMULATION PARAMETERS

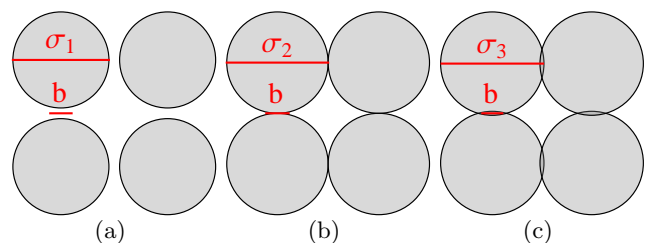


Figure 3. (Color online) Sketch of the different disk sizes σ_i for the background potential. b is the bond length. For case (a), which belongs to σ_1 , there is a finite channel between neighboring disks. (b) shows the case where neighboring disks touch each other at one point (case σ_2). As there are no bond and no monomer volume, there is still a small probability of crossing this touching point. For (c) this is no longer possible as the overlap width of neighboring disks is larger than the bond length (case σ_3).

We simulate in a square of fixed area $A = 1$ with periodic boundary conditions. The diameter of the disks is set to $\sigma_1 = 0.045$, $\sigma_2 = 0.05$ and $\sigma_3 = 0.051$. The disks are placed onto the sites of a square lattice with 20×20 sites and lattice constant $a = 0.05$. The site occupation probabilities of the lattice include $p = 0, 0.13, 0.25, 0.38, 0.51, 0.64, 0.76, 0.89, 1.00$. For $\sigma = a$, these densities correspond on average to the area fractions $\rho = 0, 0.1, 0.2, 0.3, 0.4, 0.5, 0.6, 0.7, 0.785$. The number of monomers—except for some scaling considerations—per polymer chain is $N + 1 = 30$. The monomers are considered pointlike. The bond length is set to 0.01. Accordingly, the only constraints are the fixed length of the bonds and the fact that a monomer is not allowed to be placed on a disk of the background potential. If we look more closely, we realize that for σ_1 there is a channel of half the bond length between neighboring disks [see Fig. 3(a)]. For σ_2 [Fig. 3(b)], neighboring disks of the background potential touch each other at one point. The bonds of the polymer can overlap with the disks of the background potential. As there are no monomer and no bond volume, there is a small proba-

bility of the polymer getting through the touching point of two neighboring disks. For σ_3 [Fig. 3(c)] this is no longer possible as the overlap width of neighboring disks is larger than the bond length of the polymer. This was chosen in order to compare the algorithm's ability to explore narrow channels in a high-density disorder landscape. For the case of thirty monomers, the polymer has a length of about six disk diameters if it is completely stretched.

V. RESULTS AND DISCUSSION

In our analysis we focus on three observables: the end-to-end distribution $P(r)$, the tangent-tangent correlations $\langle \mathbf{t}(0)\mathbf{t}(s) \rangle$ and the mean squared end-to-end distance $\langle R_{ee}^2 \rangle(N)$. The end-to-end distribution gives the probability for finding a certain end-to-end distance r . For a free flexible polymer, the end-to-end distribution is of the form $P(\hat{r}) \propto \hat{r} e^{-\hat{r}^2/2\sigma^2}$, where $\hat{r} = r/L$ with $L = bN$. The tangent-tangent correlation function shows the average correlation of two bonds $\mathbf{t}(i)$ and $\mathbf{t}(i+s)$. In our case it is defined by

$$\langle \mathbf{t}(0)\mathbf{t}(s) \rangle = \sum_{i=0}^{N-1-s} \frac{\mathbf{t}(i)\mathbf{t}(i+s)}{N-1-s}. \quad (7)$$

The tangent-tangent correlation function is a measure of the stiffness of the polymer. For a completely flexible polymer, the correlations are zero. The surrounding disorder can lead to both correlations and anti-correlations as can be seen in Fig. 4(c).

The last observable that we consider is the mean square end-to-end distance in dependence on the polymer length counted in numbers of bonds. In order to compare to the literature, we consider the mean square end-to-end distance without normalization. For free polymers it grows linearly in N .

The statistical errors are estimated in the standard way by calculating the variance over the disorder realizations, which are uncorrelated. In the plots we omitted the error bars as they turned out to be smaller than the plot markers.

Figure 4 is a showcase of different scenarios that can occur during the disorder averaging. Pinpoint 1 is in a small cavity that is entropically unfavorable for the polymer compared to a larger space such as can be seen around pinpoint 2. As long as the polymer has the chance to explore a larger area by escaping from a small cavity through a channel, this will happen even if the channel is extremely narrow (Fig. 5). The end-to-end distribution $P(r)$ for σ_1 and σ_2 shows this behavior, which is the same for both algorithms. It is reflected by the double-peak structure of $P(r)$ in Fig. 4(b). The small peak comes from the cavity where the polymer is pinned and the big one from the nearby free space region, which is entropically much more favorable. For the case of σ_3 —no channel left between neighboring disks—the distribution

is characterized by a single peak, which corresponds to the exploration of the tiny hole, containing pinpoint 1. The broad single peaked curve (solid black) in Fig. 4(b) belongs to pinpoint 2. For all three cases of the diameter of the background potential, the behavior is qualitatively the same. The large area around the pin point is sampled by polymer configurations, leading to a broad end-to-end distribution. Figure 4(c) shows the tangent-tangent correlations for the different pinpoints. While pinpoint 2 leads to quick decorrelation of the tangents, which is characteristic for a free polymer, things are completely different for pinpoint 1. σ_1 and σ_2 show a correlation that is due to the fact that the polymer stretches to the entropically favorable region next to pinpoint 1 through the channels between the disks. This leads to a correlation on short to intermediate lengths along the polymer. For σ_3 , where no channels are left, the polymer coils up in the cavity where it is pinned. This leads to strong anti-correlations on short length scales. For both pinpoints, the two employed simulation algorithms yield consistent results. This is reassuring since neither continuum chain-growth algorithms nor our special multicanonical method has been applied and tested before extensively.

After having looked at a single disorder realization that exhibits two exemplary cases, we move on to the case of averaging over disorder. We take about 1500 disorder realizations for the quenched average. We define the equality of the mean free path between neighboring disks and the mean end-to-end distance of the free chain to mark the crossover between a low- and a high-density regime. The effective free area per disk A_{eff} that is accessible for the polymer is

$$A_{\text{eff}} = \frac{A - pM\sigma^2\pi/4}{pM}, \quad (8)$$

with A , p and σ as described in Sec. IV and M the number of lattice sites—this is valid only for $\sigma \leq a$, where neighboring disks do not overlap. The square root of A_{eff} gives the average free path per occupied site $x(p)$. The occupation p_0 where $x(p)$ equals the mean end-to-end distance of the polymer, which is $\sqrt{\langle R_{ee}^2 \rangle} = \sqrt{Nb}$ for the free flexible case, marks the crossover

$$p_0 = (a/b)^2 \frac{1}{1 + \frac{\pi}{4}(\sigma/b)^2/N} \frac{1}{N}. \quad (9)$$

For the case considered here ($a = 0.05$, $b = 0.01$, $N = 29$), this gives $p_0 \approx 0.56$ for $\sigma = 0.045$ and $p_0 \approx 0.51$ for $\sigma = 0.05$ and $\sigma = 0.051$. Figure 6 shows the observables for a freely jointed chain for low densities of the background potential. In this regime ($p \leq p_0$), where the disorder landscape consists of free space and some randomly distributed obstacles [see Fig. 7(a)], the cases of different disk diameters $\sigma_{1,2,3}$ are similar. The end-to-end distribution [Fig. 6(a)] is characterized by a single peak that is shifted to the left and becomes more pronounced for increasing density of the background, which can be interpreted as compression of the polymer by the

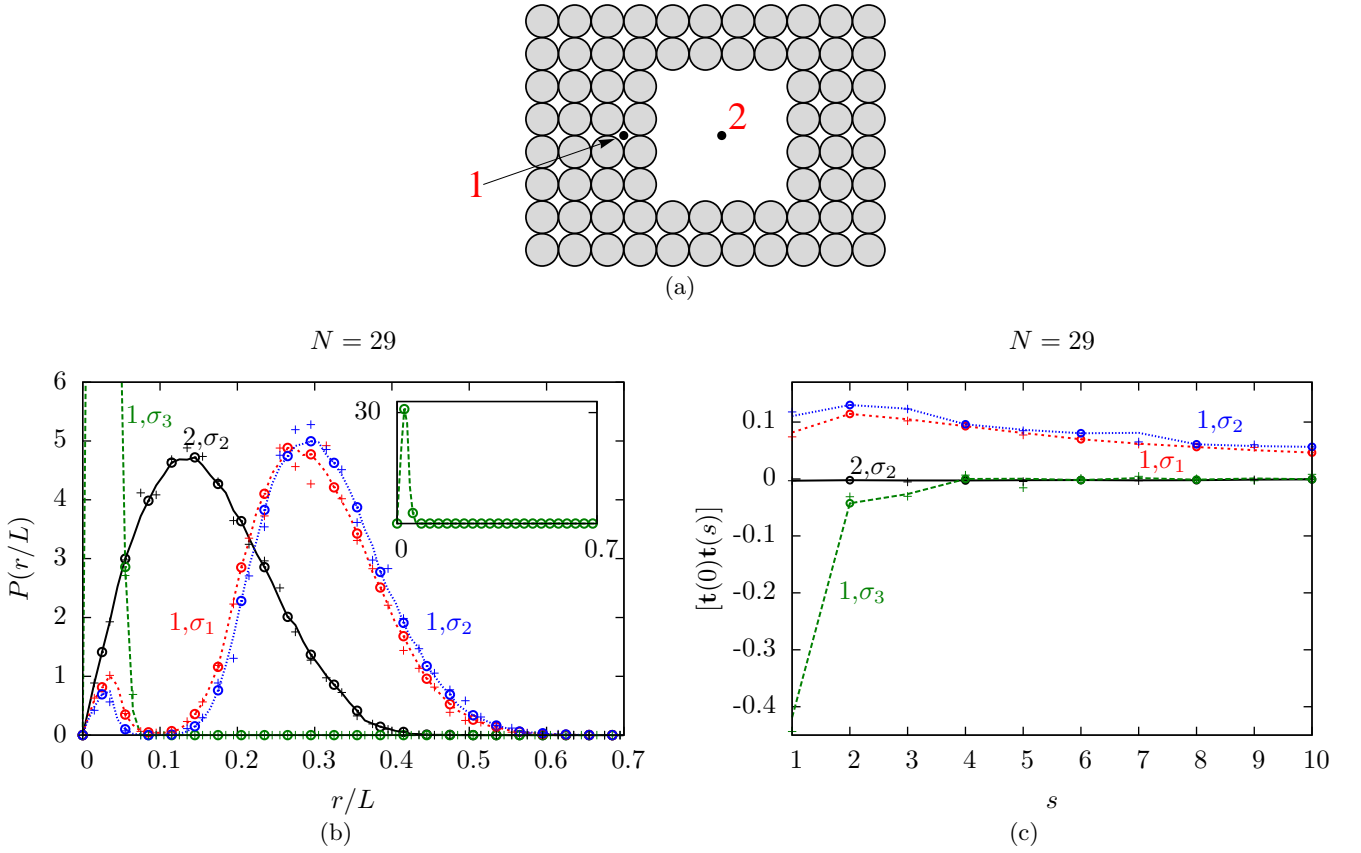


Figure 4. (Color online) (a) shows a distribution of disks with two exemplary pinpoints for polymers. All sides are continued with disks. The boundary conditions are periodic. (b) is the accordant end-to-end distribution and (c) the tangent-tangent correlation function (single simulation; no disorder average). \circ shows the data from the growth algorithm, $+$ from the multicanonical simulation. The double-peaked curves [dotted (blue) and short-dashed (red)] in (b) as well as the single peaked curve [dashed (green)], which is shown in full y range in the inset, belong to pinpoint 1. The double peaked curves belong to σ_1 [short-dashed (red)] and σ_2 [dotted (blue)]. The strongly peaked curve [dashed (green)] belongs to σ_3 . The solid (black) curve with the broad single peak belongs to pinpoint 2 for σ_2 . The curves for σ_1 and σ_3 are not shown for pinpoint 2 as they behave similarly to σ_2 . The line coding is the same for the tangent-tangent correlations (c).

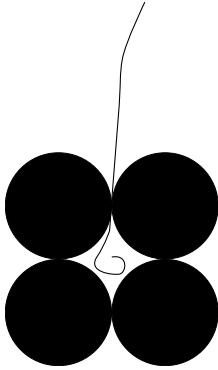


Figure 5. The sketch of a polymer that finds its way through a narrow channel to explore the large space behind.

background potential. The tangent-tangent correlations [Fig. 6(b)] show an anti-correlation for increasing density of the background potential, which goes quickly to zero correlation. This is characteristic for the free polymer. The strength of the anti-correlation is one order of magnitude weaker than for the case of high densities. The deviation of the mean square end-to-end distance from the behavior of the free case [dashed line in Fig. 6(c)] shows the influence of the potential on the polymer in reducing the space to spread out. The magnitude of the deviation from the free case is again insignificant compared to the high-density case. Computationally we observe in the low-density regime perfect agreement of the two simulation methods at the level of the line-thickness in Fig. 6.

If we increase the density, the lattice structure dominates more and more, which leads to a structure consisting of holes of different sizes [Fig. 7(b)] that finally ends in a fully occupied lattice where only tiny holes of space are left [Fig. 7(c)]. The case of intermediate and

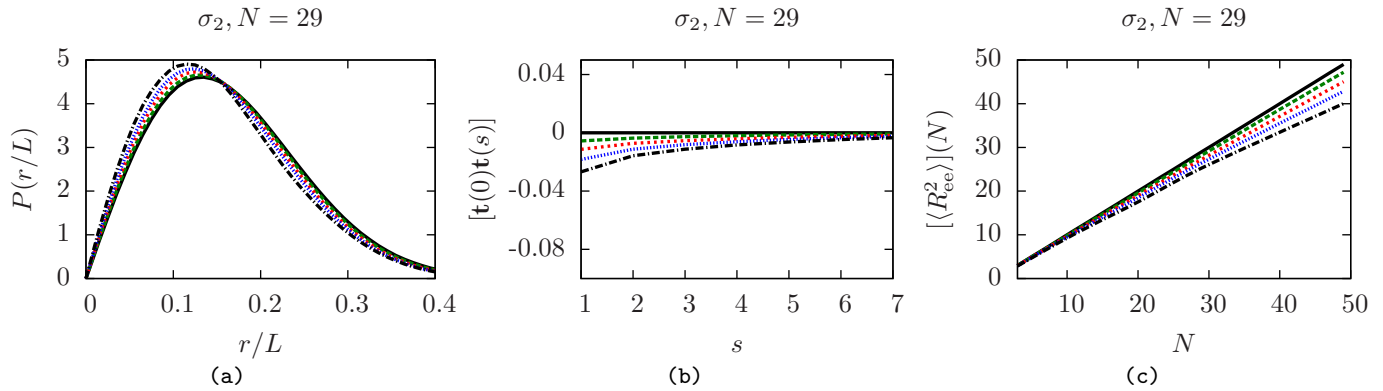


Figure 6. (Color online) (a) End-to-end distribution function for site occupation $p = 0$ (—, black solid), 0.13 (---, green), 0.25 (-.-., red), 0.38 (....., blue), and 0.51 (-.-.-, black) for increasing peak height. The curves are interpolating lines through the data (whose markers have been omitted for better visibility). The results of the two algorithms agree within the line thickness. The influence of the disk diameter σ_i is negligible in this density regime and chosen here to be σ_2 . (b) and (c) are the corresponding plots for the tangent-tangent correlations and the mean square end-to-end distance (in units of squared bond length b^2).

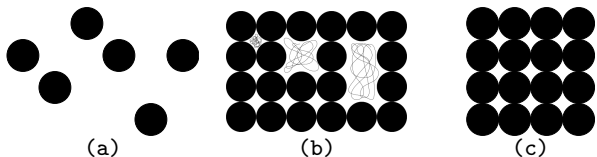


Figure 7. Disorder realizations for increasing density of the background potential from left to right. (a) Low densities consist of single disks distributed in space. (b) In the intermediate- and high-density regimes there are holes of different sizes, whereas for a fully occupied lattice (c) there are only tiny holes left that cannot be occupied by disks of the potential.

high densities ($p > p_0$) is shown in Figs. 8, 9 and 10 for the three observables. The effect of cavities and channels dominates this regime and leads to deviations depending on the choice of the diameter of the disks of the background potential σ_i .

All three cases ($\sigma_{1,2,3}$) are determined by an interplay between configurations where the pinpoint is inside a small cavity and configurations whose pinpoint is in a larger area. For $p = 1$ there finally are only small cavities left. The case of σ_3 , where the disks can overlap, is somewhat special. For one thing, the occupation $p = 0.59$ could play an important role, as this is the site percolation threshold of the square lattice. At this point, there is a percolating cluster in one direction which limits the space for chain elongation. Furthermore, a polymer whose pinpoint is inside a cavity cannot escape from it while this is possible for σ_1 and σ_2 . This effect can be well observed in the distribution of end-to-end distances. For $p = 0.64$ (long-dashed green curve in the plots of Fig. 8), σ_1 and σ_2 still show the low-density behavior, which is a single peak shifted to shorter lengths compared to the free polymer. For σ_3 , a small bulge next to the main peak

can be seen. The position of the bulge in the end-to-end distribution corresponds to an extension of the chain of the order of 1–2 bond lengths which is the extent of the tiny holes [Fig. 7(c)]. For intermediate densities it is very probable that there is a larger free area next to a small cavity. A polymer pinned inside a small cavity thus tries to escape from that region in order to reach the entropically much more favorable space. Consequently, there is no strong contribution from polymer configurations in small cavities. This is of course different for σ_3 . For $p = 0.76$ (short-dashed red curves), this effect enters also the case for σ_1 and σ_2 as there is less large space next to cavities. This reduces the gain in entropy when leaving a cavity. This is more pronounced for σ_2 as there the channels for escape are much smaller. For $p = 1$, all three cases yield qualitatively the same results again. In this case there is no more benefit in escaping a small cavity, as there are only small cavities left. For the cases of σ_1 and σ_2 the polymer thus stays in the cavities whereas for σ_3 it cannot leave the cavity at all. The tangent-tangent correlations, Fig. 9, confirm the findings for the end-to-end distribution. For high densities the polymer is coiled up in a small region and therefore in a strongly folded state. This leads to an anti-correlation of the tangents on very short length scales as in a highly folded state it is more probable to have large angles between neighboring bonds. However, this quickly averages out on longer length scales. This effect gains importance with increasing density. A further effect, which is hardly seen in the distributions of Fig. 9 as the quenched disorder average combines and thus smears different effects, is a stiffening of the polymer—that is a positive correlation of bonds—on short length scales for intermediate densities with σ_1 and σ_2 . It can well be seen for the single disorder configuration analysis in Fig. 4(c) (short-dashed red and dotted blue curves) and is already explained there. A polymer that is pinned to a small hole that is next to larger space

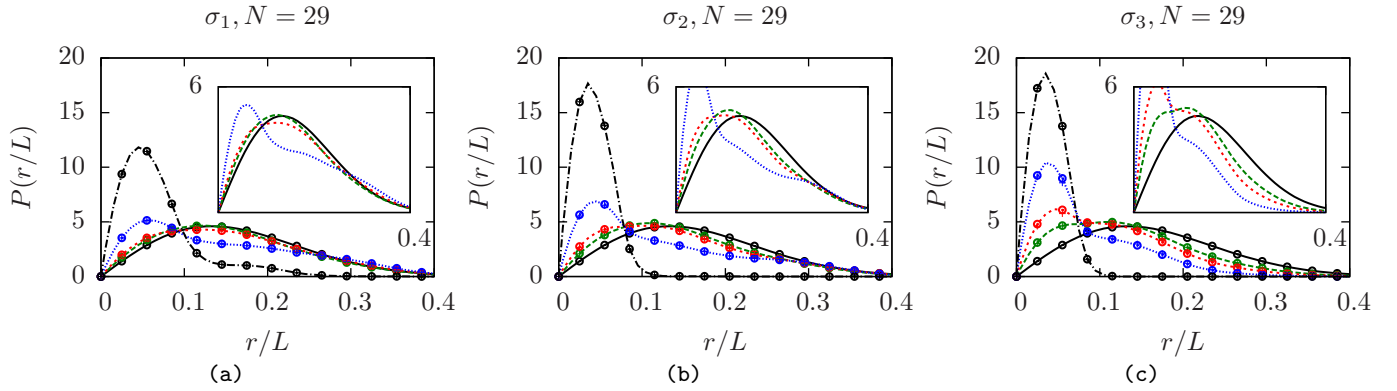


Figure 8. (Color online) End-to-end distribution function for site occupation $p = 0.64$ (---, green), 0.76 (---, red), 0.89 (---, blue), and 1 (---, black). The black solid curve is the end-to-end distribution of the free polymer as reference. The data marked by \circ are from the growth algorithm and $+$ are from the multicanonical algorithm. The different plots are made for $\sigma_{1,2,3}$. The inset shows in each case the regime $p = 0.64, 0.76, 0.89$ (the black solid curve is again the case $p = 0$ as reference), where both the influence of the low-density regime and the influence of the small cavities play a role.

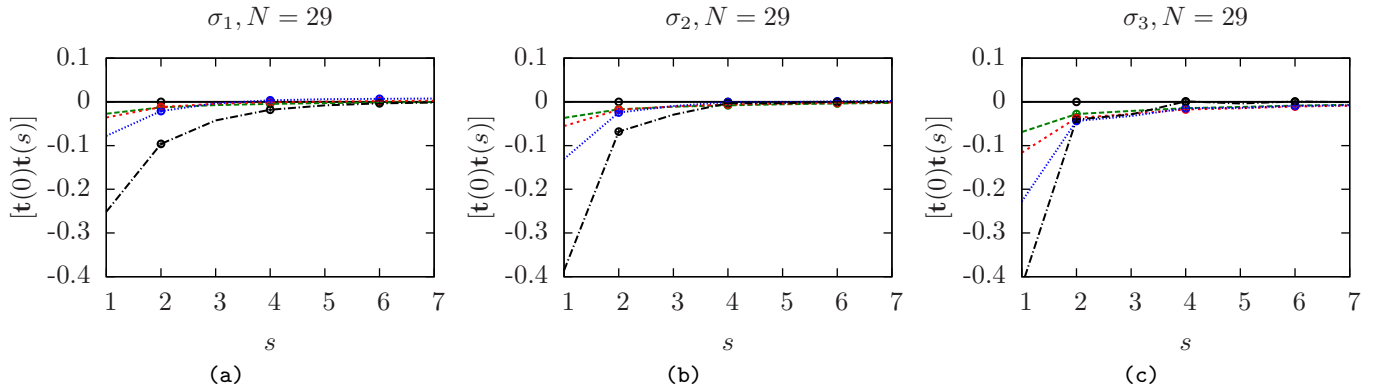


Figure 9. (Color online) Tangent-tangent correlations for $p = 0.64$ (---, green), 0.76 (---, red), 0.89 (---, blue), and 1 (---, black). The black solid curve is for $p = 0$ as reference. The data marked by \circ are from the growth algorithm, whereas $+$ come from the multicanonical algorithm. (a), (b), and (c) differ in the disk diameter. The larger the disk diameter the stronger the anti-correlations on short length scales.

stretches out to reach the entropically beneficial region which leads to the above described positive correlations of tangents. Cates and Ball [6] find similar effects due to energy instead of entropy (tadpole configurations) with pinned polymers.

The last thing to be discussed here is the mean square end-to-end distance in dependence on the number of bonds N , which is shown in Fig. 10. The chain-growth algorithm produces results in each step of growth which reduces the computational effort for estimating the scaling of the mean square end-to-end distance. By comparison with the multicanonical method we found that the potential risk of systematic errors due to correlations of shorter and longer chains can be neglected within our parameter range. For the multicanonical method, the data for each polymer length have to be generated separately. This leads to a higher computational effort in estimating the scaling of the mean square end-to-end distance. For this reason we generated fewer data points for the

multicanonical method in Fig. 10.

For the intermediate densities in Fig. 10, both algorithms again show the same behavior as described above. The surrounding obstacles limit the extension of the polymer. This effect increases for increasing disorder density, which leads to a plateau in the mean square end-to-end distance. This has also been found by Baumgärtner and Muthukumar [4]. This effect dominates for the case of σ_3 where neighboring disks leave no space for the polymer to escape [Fig. 10(c)]. Things are different for the cases of σ_1 and σ_2 [Figs. 10(a) and 10(b)]. While the first part of the curves shows the same behavior, an increase of the mean square end-to-end distance for increasing number of bonds with a slope $m < 1$, this suddenly changes to a steep slope with $m > 1$. The slope m larger than 1 is due to the reduced angular interval that is available after the polymer has left a small cavity through a narrow channel. Accordingly the polymer is forced in a certain

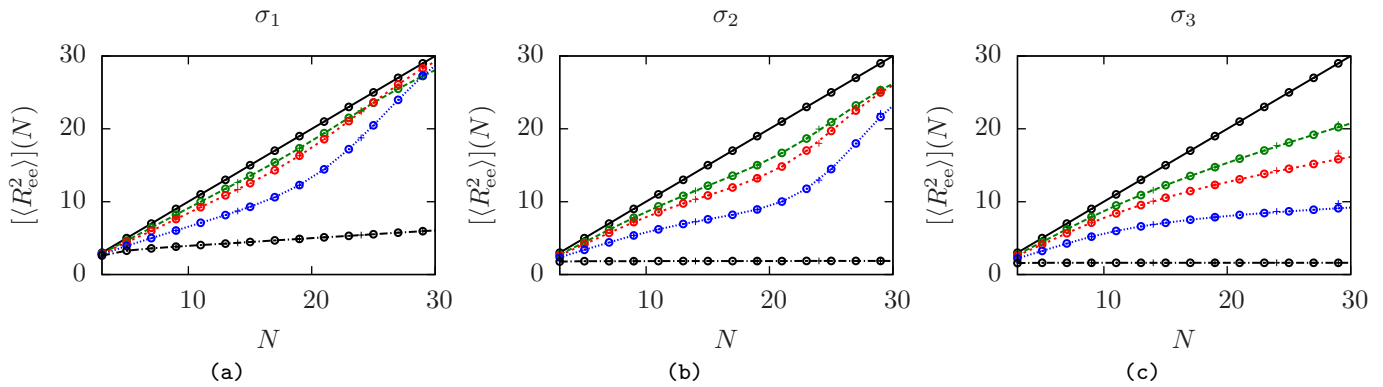


Figure 10. (Color online) Mean square end-to-end distance (in units of squared bond length b^2) for $p = 0.64$ (---, green), 0.76 (-.-., red), 0.89 (....., blue), and 1 (---, black) from top to bottom. The data marked by \circ are from the growth algorithm; $+$ come from the multicanonical algorithm. The black solid curve shows the free polymer case which scales as $[\langle R_{ee}^2 \rangle] \propto N$.

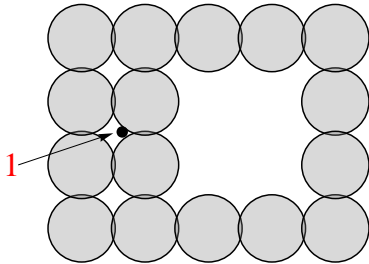


Figure 11. Hard-disk configuration and pinpoint 1 for σ_3 . For those cases the multicanonical method hardly converges as it mainly explores the area outside the cavity.

direction, which increases its extension.

After having described the phenomenology of the problem, we want to comment briefly on the algorithms for the above described problem. For the cases of σ_1 and σ_2 the two algorithms produce fully consistent results. While for shorter chain lengths the two algorithms also agree for σ_3 for high density, they start showing small deviations from each other for $N = 29$ which is barely visible only in Fig. 10(c). In analyzing the deviations, we found that this effect increases for increasing chain length. The deviations occur if a pinpoint is in a corner of a small cavity next to a larger free area. The growth algorithm explores the nearby region, building up a dense network of polymers by growing them in parallel. The multicanonical routine, however, explores space by updating an existing configuration, thereby taking into account overlaps with the surrounding disks. Afterward, these overlapping configurations are calculated out by the reweighting process. In a case as depicted in Fig. 11 there are some difficulties with this process. The space for configurations that are allowed is relatively small. As the multicanonical routine is not restricted to the allowed region, the sampling in the allowed region is very rare, which leads to convergence problems for the case of small cavities.

VI. CONCLUSION AND OUTLOOK

We investigated the phenomenology of a flexible polymer exposed to a quenched disorder landscape consisting of hard disks placed on the sites of a square lattice. We recovered the result found by Baumgärtner and Muthukumar [4] that the polymer shrinks in the presence of obstacles, which is reflected in a high probability for chains with a short end-to-end distance in the end-to-end distribution function. For high densities we found a dependency of the characteristics of the polymer on the microscopic structure of the disorder. Obstacles that leave no channels between neighboring sites lead to a plateau for all densities in the scaling of the mean square end-to-end distance for increasing numbers of bonds. This effect is inverted for the case of channels between neighboring disks. The mean square end-to-end distance shows a steep slope for intermediate to high densities as long as the polymer benefits from the channels by being able to explore entropically favorable regions.

We cross-checked our findings by applying two conceptually very different simulation algorithms: a continuum chain-growth algorithm with population control and the multicanonical method based on Markov chains in a generalized ensemble. In doing so we found very good agreement in almost all situations. Only for certain cases of high densities and subtle structures did we encounter problems with the multicanonical method.

After having checked our methods within a system that could be well controlled, we mean to apply them to more sophisticated disorder landscapes such as hard-disk fluids. Also, the polymer model can be adapted such that it includes bending terms which makes it applicable to biological polymer systems. Those are often modeled by the worm-like chain.

ACKNOWLEDGMENTS

We gratefully thank Sebastian Sturm, Niklas Fricke, and Mathias Aust for discussion and beneficial advice

about the problem addressed here. The project was financially supported by the Leipzig Graduate School of Excellence GSC 185 “BuildMoNa” and the Deutsch-Französische Hochschule (DFH-UFA).

-
- [1] G. Guillot, L. Leger, and F. Rondelez, *Macromolecules* **18**, 2531 (1985).
 - [2] D. S. Cannell and F. Rondelez, *Macromolecules* **13**, 1599 (1980).
 - [3] M. T. Bishop, K. H. Langley, and F. E. Karasz, *Phys. Rev. Lett.* **57**, 1741 (1986).
 - [4] A. Baumgärtner and M. Muthukumar, *J. Chem. Phys.* **87**, 3082 (1987).
 - [5] S. F. Edwards and M. Muthukumar, *J. Chem. Phys.* **89**, 2435 (1988).
 - [6] M. E. Cates and R. C. Ball, *J. Phys. France* **49**, 2009 (1988).
 - [7] J. Machta, *Phys. Rev. A* **40**, 1720 (1989).
 - [8] T. Nattermann and W. Renz, *Phys. Rev. A* **40**, 4675 (1989).
 - [9] Y. Y. Goldschmidt, *Phys. Rev. E* **61**, 1729 (1999).
 - [10] Y. Y. Goldschmidt and Y. Shiferaw, *Eur. Phys. J. B* **32**, 87 (2003).
 - [11] S. Stepanow, *J. Phys. A* **25**, 6187 (1992).
 - [12] J. Machta and T. R. Kirkpatrick, *Phys. Rev. A* **41**, 5345 (1990).
 - [13] V. Blavatska and W. Janke, *J. Phys. A* **42**, 015001 (2009).
 - [14] J. D. Honeycutt and D. Thirumalai, *J. Chem. Phys.* **80**, 4542 (1989).
 - [15] S. Schöbl and W. Janke, Leipzig preprint, in preparation.
 - [16] T. Garel and H. Orland, *J. Phys. A* **23**, L621 (1990).
 - [17] P. Grassberger, *Phys. Rev. E* **56**, 3682 (1997).
 - [18] M. Bachmann and W. Janke, *Phys. Rev. Lett.* **95**, 058102 (2005).
 - [19] V. Blavatska and W. Janke, *Europhys. Lett.* **82**, 66006 (2008).
 - [20] V. Blavatska and W. Janke, *Phys. Rev. Lett.* **101**, 125701 (2008).
 - [21] B. A. Berg and T. Neuhaus, *Phys. Lett. B* **267**, 249 (1991).
 - [22] B. A. Berg and T. Neuhaus, *Phys. Rev. Lett.* **68**, 9 (1992).
 - [23] W. Janke, *Physica A* **254**, 164 (1998).
 - [24] C. Junghans, M. Bachmann, and W. Janke, *Phys. Rev. Lett.* **97**, 218103 (2006).
 - [25] N. Metropolis, A. W. Rosenbluth, M. N. Rosenbluth, A. H. Teller, and E. Teller, *J. Chem. Phys.* **21**, 1087 (1953).